Vacuum 155 (2018) 594–603

Contents lists available at ScienceDirect

Vacuum

journal homepage: www.elsevier.com/locate/vacuum

Effects of Ce addition on the Cu-Mg-Fe alloy hot deformation behavior

Bingjie Wang[a,b], Yi Zhang[a,b,*], Baohong Tian[a,b,*], Junchao An[b,c,*], Alex A. Volinsky[d], Huili Sun[a,b], Yong Liu[a,b], Kexing Song[a,b]

[a] School of Materials Science and Engineering, Henan University of Science and Technology, Luoyang, 471023, PR China
[b] Collaborative Innovation Center of Nonferrous Metals, Henan Province, Luoyang, 471023, PR China
[c] School of Materials Science and Engineering, Luoyang Institute of Science and Technology, Luoyang, 471023, PR China
[d] Department of Mechanical Engineering, University of South Florida, Tampa, 33620, USA

ARTICLE INFO

Keywords:
Cu-Mg-Fe-Ce alloy
Hot deformation
Flow stress
Dynamic recrystallization
Constitutive equations

ABSTRACT

The effects of Ce addition on the Cu-Mg-Fe alloy hot deformation process were investigated through the isothermal compression tests using the Gleeble-1500D thermo-mechanical simulator at 500–850 °C temperature range and 0.001–10 s^{-1} strain rate range. The interaction of work hardening, dynamic recovery and dynamic recrystallization during plastic deformation was studied, and the constitutive equations of Cu-Mg-Fe and Cu-Mg-Fe-Ce alloys were established. The addition of Ce can delay the occurrence of dynamic recrystallization, enhance the flow stress and apparently narrow the unstable domain during hot deformation process of the Cu-Mg-Fe alloy. Two optimal hot working parameters for the Cu-Mg-Fe alloy are obtained. The first is temperature of 650–800 °C and strain rate of 0.001–0.01 s^{-1}, and the second is temperature of 775–850 °C and strain rate of 0.01–0.6 s^{-1}. The optimal hot working parameters for the Cu-Mg-Fe-Ce alloy are 675–850 °C and strain rate of 0.01–0.4 s^{-1}. The precipitate of the Cu-Mg-Fe-Ce alloy deformed at 850 °C and 0.001 s^{-1} was determined to be $CuMg_2$. $CuMg_2$ precipitation can improve the hardness and hot deformation activation energy of the Cu-Mg-Fe alloy. Meanwhile, the addition of Ce can promote the precipitation of $CuMg_2$.

1. Introduction

Demand for high-performance conductors has recently increased with the development of high-speed trains. Accordingly, requirements for the performance of electric contact wires have been raised. Copper alloys , such as Cu-Zr-Cr, Cu-Ag-Cr, Cu-Mg, Cu-Sn and Cu-Ag have been widely used for contact electrical wire due to their excellent physical and mechanical properties, including high electrical conductivity and high temperature oxidation resistance [1–3]. Zhang et al. [4] studied the effects of Ce on the hot deformation behavior of the Cu-Zr-Cr alloy and found that Ce produces grain refinement and increases the flow stress of the alloy. Zhang et al. [5] also concluded that the addition of Ce to Cu-Zr alloy improves hot deformation domains during hot deformation. Dai at al. [6] analyzed Ce effects on the non-vacuum melting process of Cu-Cr-Zr alloy and proved that the addition of Ce can eliminate pine-tree crystals, create fine grains and clear grain boundaries. Liu et al. [7] studied Cu-0.1%Ag-0.06%Ce alloy and demonstrated that Ce addition can improve strength, hardness and provide resistance to softening.

Cu-Mg alloy contact wire is currently one of the most widely used contact wires. The burning loss of magnesium is very serious in the smelting process, which can cause uneven distribution of the elements and lead to coarse grains. The addition of proper amounts of rare elements can reduce the number of inclusions in the metal matrix, thus refining the grains [8]. The main purpose of this study is to investigate hot deformation behavior and effects of the addition of Ce on the Cu-Mg-Fe alloy matrix by isothermal compression tests. The relationships between the flow stress, deformation temperatures and strain rates were obtained. The microstructure evolution under various conditions was analyzed. Furthermore, the constitutive equations and processing maps were established. Subsequently, the activation energy and optimized hot working parameters were determined.

2. Experimental procedures

Chemical composition (wt.%) of the Cu-Mg-Fe and Cu-Mg-Fe-Ce alloys is presented in Table 1. The experimental alloys were cast in the ZG-0.01 vacuum medium frequency induction melting furnace in a graphite crucible in argon at 1200 °C. Prior to melting, the mold was preheated to 200 °C to keep it dry. Pure Cu, Mg, Sn and master alloys Cu-10%Fe, Cu-12%P, Cu-19%Ce were used. These were poured into a low carbon steel mold with Φ85 mm × 120 mm dimensions. The as-cast

---

[*] Corresponding authors. School of Materials Science and Engineering, Henan University of Science and Technology, Luoyang, 471023, PR China.
E-mail addresses: zhshgu436@163.com (Y. Zhang), tianbh@haust.edu.cn (B. Tian), superjun@tju.edu.cn (J. An).

https://doi.org/10.1016/j.vacuum.2018.06.006
Received 9 April 2018; Received in revised form 1 June 2018; Accepted 1 June 2018

Table 1
Chemical composition of the Cu-Mg-Fe and Cu-Mg-Fe-Ce alloys (wt.%).

Alloy	Mg	Fe	Sn	P	Ce	Cu
Cu-Mg-Fe	0.4	0.2	0.2	0.15	–	Bal.
Cu-Mg-Fe-Ce	0.4	0.2	0.2	0.15	0.15	Bal.

ingots were then extruded into bars of 35 mm diameter using the XJ-500 metal profile extrusion machine at 900 °C for 2 h and then air cooled. The schematic illustration of the complete test is shown in Fig. 1. The deformed specimens with Φ8 mm x 12 mm dimensions were compressed by the Gleeble-1500D thermo-mechanical simulator. Prior to compression, the samples were heated to the experimental temperature at 10 °C/s rate and then kept at test temperature for about 3 min, and subsequently compression tested. Water was used as the cooling medium to obtain the high temperature deformed microstructure. The samples were carved perpendicular to the direction of deformation. The central part of the specimens were polished and then chemically etched with $FeCl_3$ (5 g) + HCl (10 mL) + distilled water (100 mL) and the microstructure was observed using OLYMPUS PMG3 optical microscope. The specimen was processed into a wafer with a thickness of 50 μm and a diameter of 3 mm, and subsequently ion thinned using Gatan 691 ion beam thinner. High resolution transmission electron microscope (HRTEM, JEM-2100) was used to characterize the precipitated phase. The hardness of the experimental alloys after high temperature extrusion was measured by the HVS-1000 A hardness tester. Each sample was measured 8 times to obtain an average value, and measurement error was calculated statistically to be 10%.

3. Results and discussion

Fig. 2(a) and Fig. 2(b) demonstrate the as-cast microstructure of the Cu-Mg-Fe and Cu-Mg-Fe-Ce alloys, where multiple coarse dendritic grains were observed in the ingot. Nevertheless, the grains of the Cu-Mg-Fe-Ce alloy are finer than the Cu-Mg-Fe alloy with the average grain size of 179.5 μm and 353.3 μm, respectively. This indicates that the addition of Ce can refine the grains. Fig. 2(c) is the microstructure of the Cu-Mg-Fe-Ce alloy extruded at 900 °C. It was observed that the dendrite structure disappeared and many grains became finer with an average grain size of 48.2 μm after extrusion. Fig. 2(d) shows the average hardness of the two alloys after extrusion. Hardness of the Cu-Mg-Fe alloy is 75 HV, while the hardness of the Cu-Mg-Fe-Ce alloy is 90 HV, which is about 19% higher. This implies that the addition of Ce has a positive effect on improving the alloy hardness.

Fig. 3 shows scanning electron micrographs of the Cu-Mg-Fe-Ce alloy after high temperature extrusion. Fig. 3(a) is the micrograph of the matrix. Energy dispersive spectra, corresponding elements and composition of the extruded alloy are shown in Fig. 3(b). It can be seen from the energy spectra that the added Mg, Fe, Sn, Ce and P are distributed throughout the matrix.

3.1. True stress-true strain curves

Plastic deformation consists of work hardening, dynamic recovery (DRV) and dynamic recrystallization (DRX) [9,10]. Fig. 4 shows the true stress-true strain curves of the Cu-Mg-Fe and Cu-Mg-Fe-Ce alloys obtained at different temperatures and various strain rates. All curves exhibit similar trends, which are related to deformation temperature and strain rate. The flow stress increases with lower temperature or higher strain rate.

Plastic deformation can increase dislocation density. The proliferation and entanglement of dislocations lead to work hardening. Thus, the flow stress increased rapidly with the true strain at the initial stage of hot deformation process. High dislocation density induced by hot deformation is the dominant mechanism responsible for the high work hardening [11,12]. Ji et al. [13] studied the hot deformation behavior of the Cu-0.4%Mg alloy and found that the flow stress increases with the strain rate. Meanwhile, it represents typical characteristics of DRV and DRX. Furthermore, DRV and DRX are related to the work hardening rate. Mirzadeh et al. analyzed the flow curves of 17–4 PH stainless steel [14] and verified that it was inadequate to judge DRV or DRX according to the shape of flow stress curves. Work hardening rate analysis can accurately determine whether DRV or dynamic DRX occurs [15,16]. Based on the carbon microalloyed steel and NiTi intermetallic compound during hot deformation, a similar conclusion has been obtained by Mirzadeh et al. [17,18].

Based on Fig. 4(a), the studied alloys deformed at 500 °C exhibited continuous working hardening. As illustrated in Fig. 5(a), the grains of the Cu-Mg-Fe-Ce alloy deformed at 500 °C and 0.001 s^{-1} are extensively elongated perpendicularly to the compressed direction and the dislocation density at the grain boundaries increased rapidly. DRV and DRX occurring simultaneously exhibit dynamic softening, which eliminates the effects of dislocations [19,20]. As temperature increases, such as 800 °C, dynamic recrystallization is the main mechanism. As shown in Fig. 5(b), a substantial number of uniform equiaxed grains are found in the copper matrix, which indicates that the alloy is in the dynamic recrystallization stage under this condition. After a rapid rise to the peak value, the flow stress decreases until a steady value is reached. More pronounced dynamic recrystallization can be observed at a higher temperature of 850 °C. This phenomenon can be observed in Fig. 4(b) and (c). Compared with the true stress-true strain curves of the

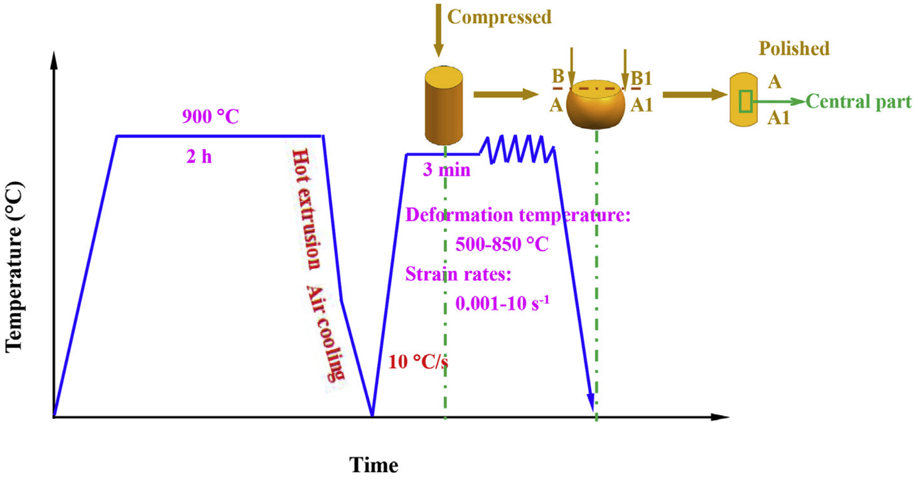

Fig. 1. Schematic illustration of thermal extrusion and hot compression deformation tests.

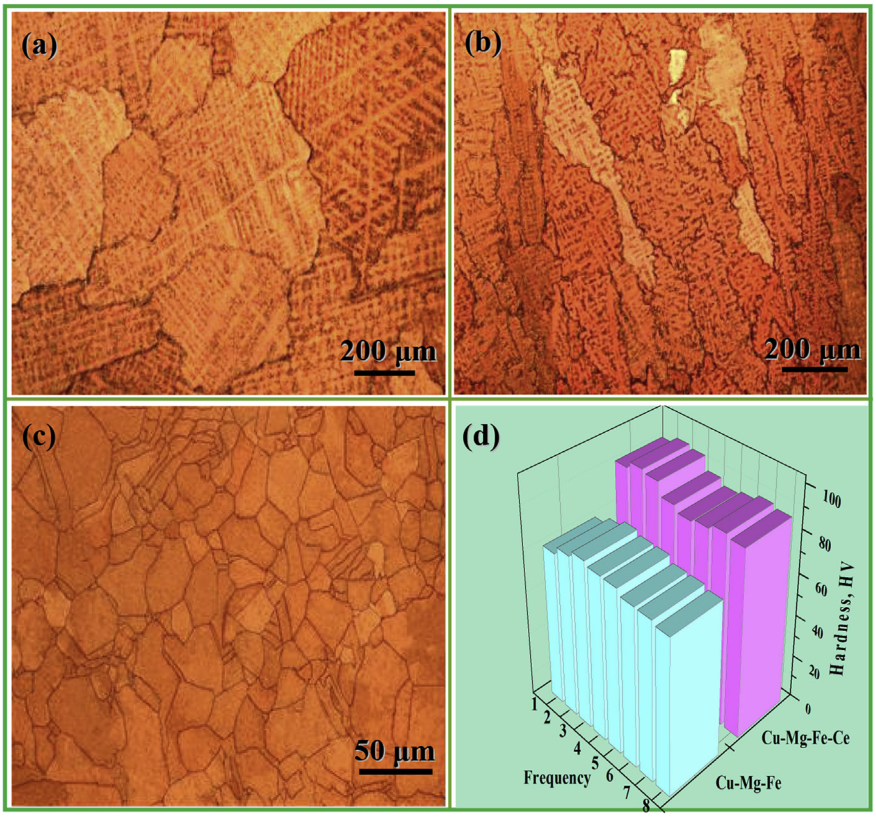

Fig. 2. Microstructure of the Cu-Mg-Fe and Cu-Mg-Fe-Ce alloys under different hot deformation conditions: (a) as-cast Cu-Mg-Fe alloy; (b) as-cast Cu-Mg-Fe-Ce alloy; (c) Cu-Mg-Fe-Ce alloy extruded at 900 °C; (d) hardness of the Cu-Mg-Fe and Cu-Mg-Fe-Ce alloys extruded at 900 °C.

Cu-Mg-Fe-Ce alloy in Fig. 4(d) obtained at higher strain rate of 1 s^{-1}, it can be clearly seen that work hardening dominates the deformation process at 500–700 °C with constant strain rate. There is no appearance of dynamic recrystallization until the temperature is raised to 850 °C. This indicates that dynamic recrystallization mainly occurs at high temperature and low strain rate. Lei et al. [21] have observed a similar phenomenon for the Cu-8.0Ni-1.8Si alloy. There is also a positive correlation between the flow stress and the strain rate. For example, when deformed at 600 °C, the true stress of the two alloys with a strain rate of 1 s^{-1} is obviously higher than with 0.1 s^{-1} strain rate, as seen in Fig. 4. However, when the strain rate is fixed, the relationship between true stress and temperature is negative [22–24]. For instance, true stress of the two alloys deformed at 700 °C significantly exceeds the value at 600 °C. This implies that the true stress increases with the strain rate.

Furthermore, compared with the Cu-Mg-Fe alloy, it is seen that the flow stress of the Cu-Mg-Fe-Ce alloy is higher than the Cu-Mg-Fe alloy under the same deformation conditions. The addition of Ce plays a significant role in strengthening the alloy matrix. For example, the peak stress of the Cu-Mg-Fe alloy is 147.5 MPa deformed at 700 °C and 1 s^{-1}, while the corresponding value of the Cu-Mg-Fe-Ce alloy is 158.3 MPa, which is about 7.3% higher than the Cu-Mg-Fe alloy. The reason for the effect is that Ce can form an oxide, which inhibits the dislocation motion and causes grain boundary pinning. Liu et al. [25] carried out EDS analysis of the Cu-Cr-Zr-Ce alloy during hot deformation and confirmed the existence of CeO_2 compound precipitated in the grain boundaries. Moreover, Ce promotes the precipitation of the secondary phase, which has a similar effect as CeO_2. Consequently, under the combined function of the secondary phase and the oxide, the true stress increases and creates a positive reinforcement of the alloy. Fig. 6(a) illustrates the TEM microstructure of the Cu-Mg-Fe alloy deformed at 700 °C and

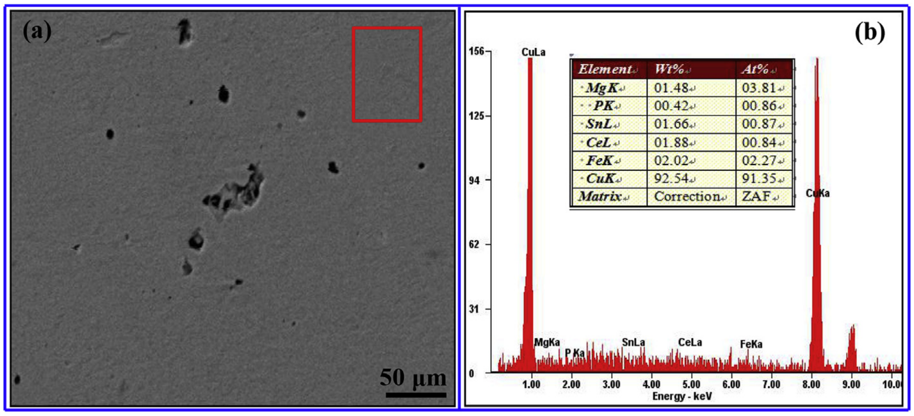

Element	Wt%	At%
MgK	01.48	03.81
PK	00.42	00.86
SnL	01.66	00.87
CeL	01.88	00.84
FeK	02.02	02.27
CuK	92.54	91.35
Matrix	Correction	ZAF

Fig. 3. (a) Microstructure and (b) EDS pattern of the Cu-Mg-Fe-Ce alloy after extrusion at 900 °C.

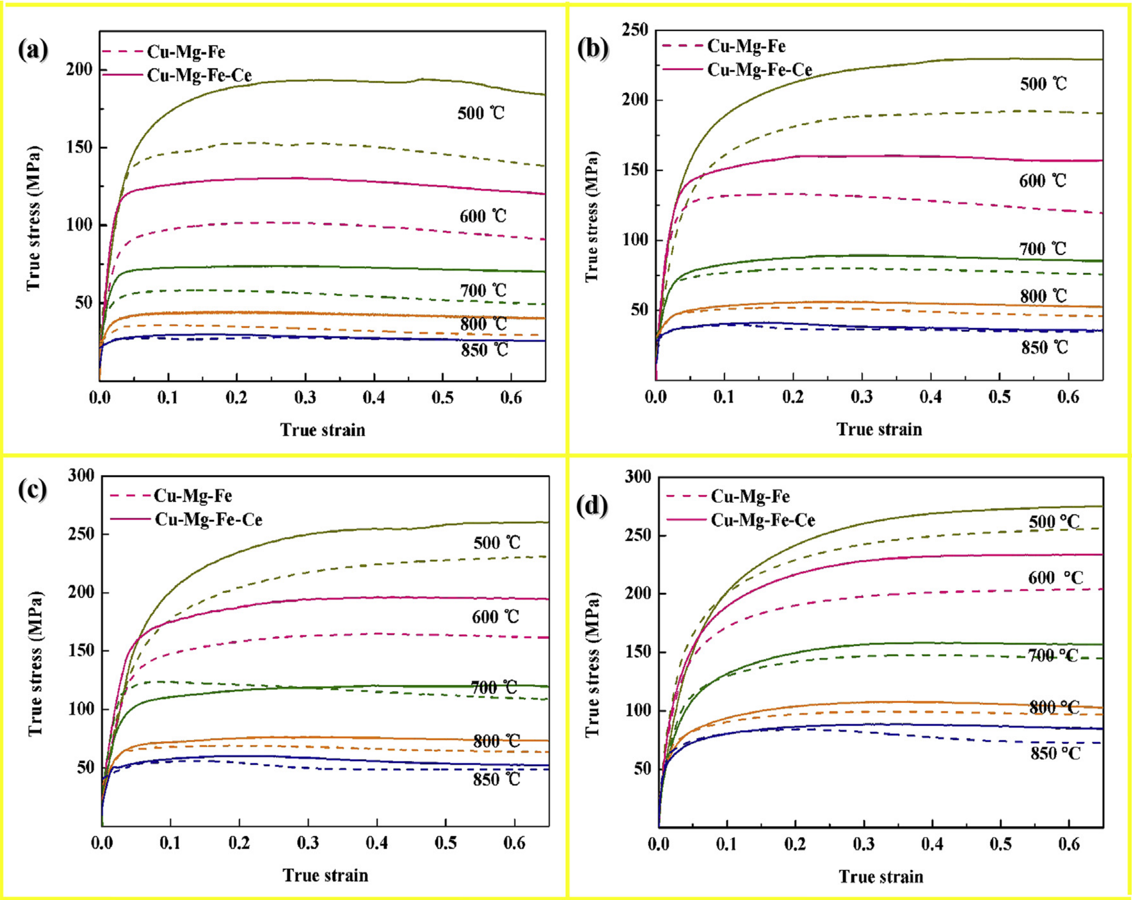

Fig. 4. True stress-true strain curves of the Cu-Mg-Fe and Cu-Mg-Fe-Ce alloys deformed at different temperatures and strain rates: (a) 0.001 s^{-1}; (b) 0.01 s^{-1}; (c) 0.1 s^{-1}; (d) 1 s^{-1}.

0.001 s^{-1}. It is seen that the matrix is mainly composed of dislocation structures. Compared with the Cu-Mg-Fe-Ce alloy, Fig. 6(b) illustrates that the amount of the secondary phase increases significantly under the same conditions. This phenomenon also indicates that the addition of Ce element promotes the precipitation of the secondary phase.

3.2. Constitutive equation

During hot deformation, flow stress mainly depends on the deformation temperature and the strain rate. Constitutive equation is applied to define the specific mathematical relationship among flow stress, deformation temperature and strain rate, which can be expressed as follows:

$$\dot{\varepsilon} = A_1\sigma^{n_1}\exp\left[-\frac{Q}{RT}\right] \quad \alpha\sigma < 0.8 \tag{1}$$

$$\dot{\varepsilon} = A_2\exp(\beta\sigma)\exp\left[-\frac{Q}{RT}\right] \quad \alpha\sigma > 1.2 \tag{2}$$

$$\dot{\varepsilon} = A[\sinh(\alpha\sigma)]^{n}\exp\left[-\frac{Q}{RT}\right] \quad \text{(For all)} \tag{3}$$

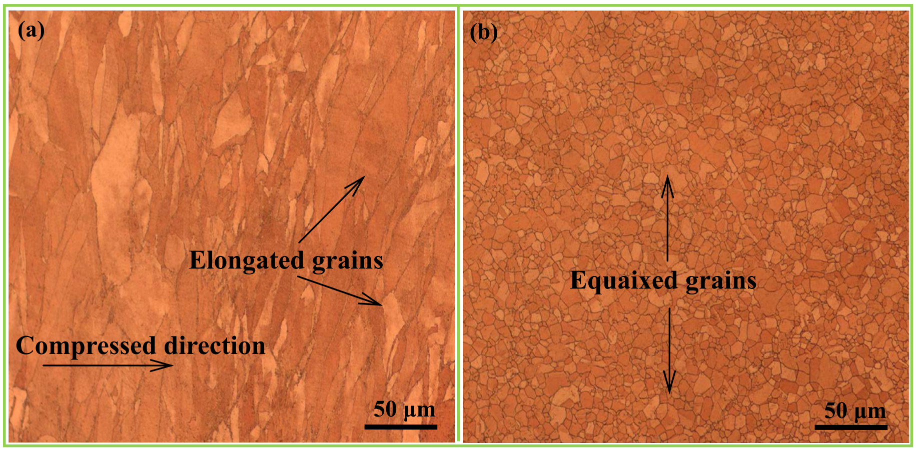

Fig. 5. Microstructure of Cu-Mg-Fe-Ce alloy defoermed at (a) 500 °C, 0.001 s^{-1}; (b) 800 °C, 0.001 s^{-1}.

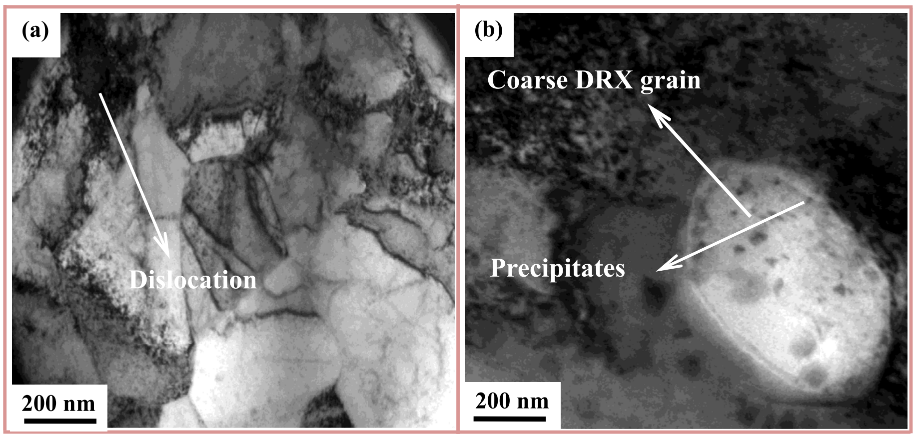

Fig. 6. TEM microstructure of (a) Cu-Mg-Fe alloy; (b) Cu-Mg-Fe-Ce alloy deformed at 700 °C and 0.001 s^{-1}.

Eq. (3) is the hyperbolic sinusoidal model proposed by Sellars and is widely used to represent the connection of the three variables [12,26]. The Zener-Hollomon parameter [26–28] is used to describe the effect of temperature and strain rate on the flow stress. Mirzadeh et al. [29] investigated the hot deformation of Mg-3Gd-1Zn magnesium alloy and 7075 Aluminum [30], and the values of the peak stress were used to calculate the constitutive equations. Related research shows that the value of Z is based on the lattice self diffusion activation energy due to dislocation slip and climb [31–33].

$$Z = \dot{\varepsilon}\exp\left[\frac{Q}{RT}\right] \tag{4}$$

Here, $\dot{\varepsilon}$ is the strain rate (s^{-1}), σ is the peak flow stress (MPa), Q represents the thermal activation energy (J/mol), A, A_1, A_2, α, β, n_1 and n are material constants, T is the temperature (K), and R is the universal gas constant (8.314 J/mol K). Taking the logarithms of both sides of Eqs. (1)–(3) yields:

$$\ln\dot{\varepsilon} = n_1\ln\sigma + \ln A_1 - \frac{Q}{RT} \tag{5}$$

$$\ln\dot{\varepsilon} = \beta\sigma + \ln A_2 - \frac{Q}{RT} \tag{6}$$

$$\ln\dot{\varepsilon} = n\ln[\sinh(\alpha\sigma)] - \frac{Q}{RT} + \ln A \tag{7}$$

Taking the Cu-Mg-Fe-Ce alloy as an example. As seen in Fig. 7(a) and Fig. 7(b), relationships between $\ln\dot{\varepsilon}$ and $\ln\sigma$, $\ln\dot{\varepsilon}$ and σ are obtained, yielding the values of n_1 and β, respectively, by taking the average of each slope, $n_1 = 8.058$, $\beta = 0.084$ MPa. Then $\alpha = \beta/n_1 = 0.010$. Then the value of n is the average of slopes in Fig. 7(c), $n = 6.928$. Suppose $\dot{\varepsilon}$ is a constant, then the deformation activation energy isdefined as:

$$Q = R\left[\frac{\partial(\ln\dot{\varepsilon})}{\partial\ln[\sin(\alpha\sigma)]}\right]_T\left[\frac{\partial\ln[\sinh(\alpha\sigma)]}{\partial(1/T)}\right]_{\dot{\varepsilon}} = RnS \tag{8}$$

According to Fig. 7(d), S is defined as the slope of $\ln Z - 1000/T$, $S = 5.621$. Therefore, hot deformation activation energy of the Cu-Mg-Fe-Ce alloy is $Q = 323.7$ kJ/mol.

Fig. 7(e) shows a linear relationship between $\ln Z$ and $\ln[\sinh(\alpha\sigma)]$. Taking logarithm of both sides of Eq. (4) yields:

$$\ln z = n\ln[\sinh(\alpha\sigma)] + \ln A \tag{9}$$

The value of A is calculated as $A = e^{34.591}$. With the same principle, parameters for the Cu-Mg-Fe alloy were obtained as follows: $\alpha = 0.013$, $n = 5.462$, $A = e^{25.612}$. Hot deformation activation energy of the Cu-Mg-Fe alloy is determined to be 255.3 kJ/mol. Thus the constitutive equations for the Cu-Mg-Fe and Cu-Mg-Fe-Ce alloys can be expressed as following:

For the Cu-Mg-Fe alloy:

$$\dot{\varepsilon} = e^{25.612}[\sinh(0.013\sigma)]^{5.462}\exp\left(-\frac{255.3}{RT}\right)$$

For the Cu-Mg-Fe-Ce alloy:

$$\dot{\varepsilon} = e^{34.591}[\sinh(0.010\sigma)]^{6.928}\exp\left(-\frac{323.7}{RT}\right)$$

Deformation activation energy of the Cu-Mg-Fe and Cu-Mg-Fe-Ce alloys is 255.3 kJ/mol and 323.7 kJ/mol, respectively, as shown in Fig. 7(f). The activation energy of the Cu-Mg-Fe alloy is lower than the Cu-Mg-Fe-Ce alloy by about 25%. The reason for this phenomenon is that Ce can promote secondary phase precipitation. The higher activation energy is the threshold stress caused by the existence of precipitates, which reduces the effective stress required for the hot deformation [34]. Meanwhile, the secondary phase and the CeO_2 compounds are distributed in the copper matrix and grain boundaries and inhibit dislocation motion. The formation of entanglements and other dislocations makes the process of plastic deformation more difficult. Thus, the deformation activation energy is increased. In addition, the refinement of rare earth elements causes an increase in grain boundary area and makes the microstructure more even. Due to the grain refinement, the interface and the resistance of dislocation movement is increased. Then the deformation activation energy increases [35].

3.3 Hot processing maps

To identify the optimized hot working conditions for the specimens, hot processing maps were established, based on the dynamic materials model. Meanwhile, both stable and unstable regions were distinguished. Prasad et al. [36–38] developed this model by means of irreversible thermodynamic theory and extremum principles. During the process of hot deformation of the experimental alloy, total power of the system is divided into two parts, represented by G and J, respectively. G represents the power applied for plastic work, while J stands for the microstructure evolution. Thus, the relation between P, G, and J is given as:

$$P = G + J = \sigma\dot{\varepsilon} = \int_0^{\dot{\varepsilon}}\sigma d\dot{\varepsilon} + \int_0^{\sigma}\dot{\varepsilon}d\sigma \tag{10}$$

In this experiment, the strain rate sensitivity parameter (m) is determined as:

$$m = \frac{dJ}{dG} = \left(\frac{\partial(\ln\sigma)}{\partial(\ln\dot{\varepsilon})}\right)_{\dot{\varepsilon},T} \tag{11}$$

For an ideal linear power dissipation, $m = 1$, and J reached the

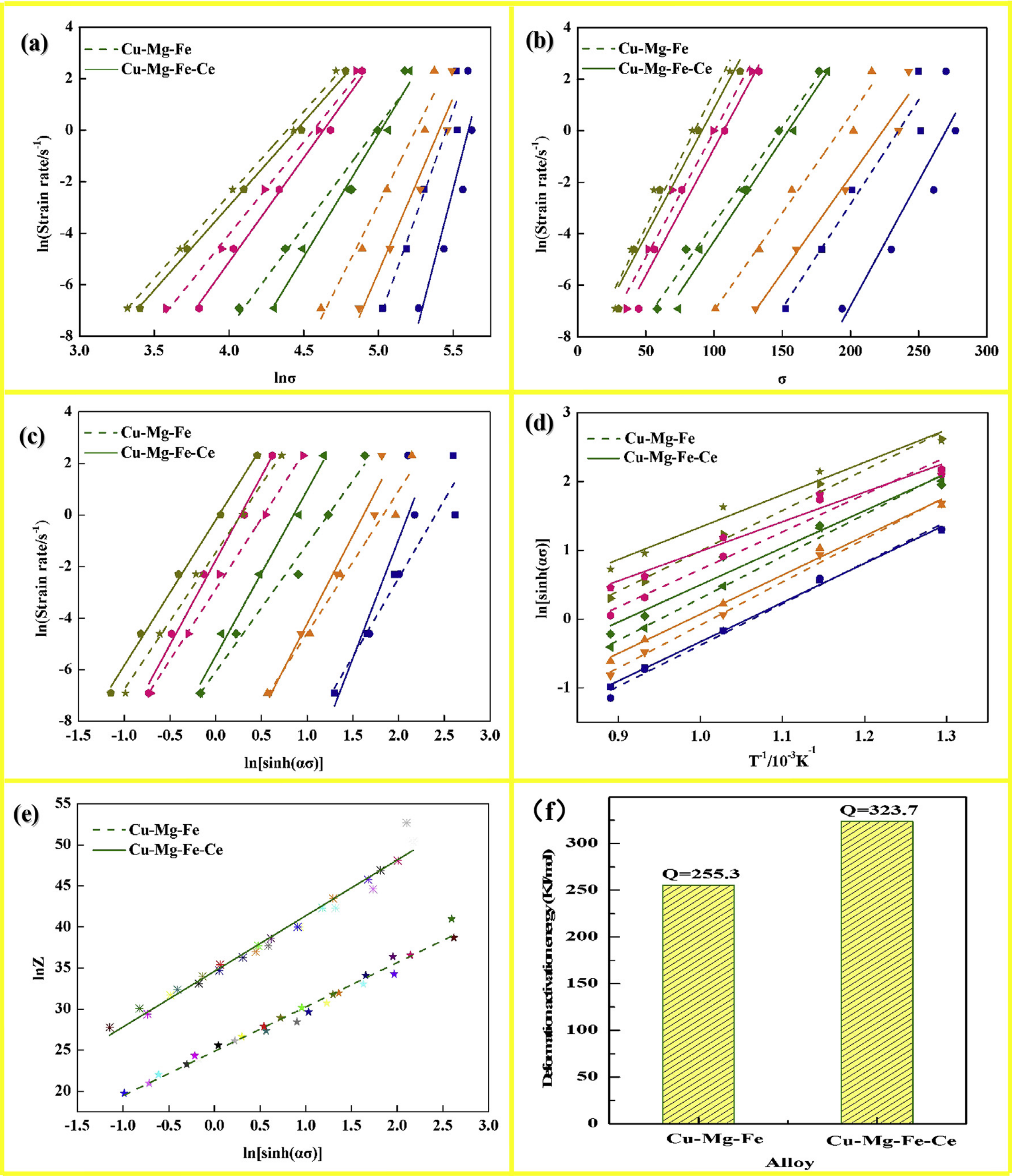

Fig. 7. Relations between: (a) $\ln\dot{\varepsilon}$ and $\ln\sigma$; (b) $\ln\dot{\varepsilon}$ and σ; (c) $\ln\dot{\varepsilon}$ and $\ln[\sinh(\alpha\sigma)]$; (d) $\ln[\sinh(\alpha\sigma)]$ and $\mathrm{T}^{-1}/10^{-3}$; (e) $\ln Z$ and $\ln[\sinh(\alpha\sigma)]$; (f) deformation activation energy of the Cu-Mg-Fe and Cu-Mg-Fe-Ce alloys.

maximum value, $J_{\max} = \sigma\dot{\varepsilon}/2 = P/2$. Assuming η represents the efficiency of power dissipation, as J reaches its maximum value, while η is determined as:

$$\eta = \frac{J}{J_{\max}} = \frac{2m}{m+1} \tag{12}$$

The value of η can indirectly reflect the processability of the experimental alloy under given conditions. The power dissipation value indicates the ratio of energy to total energy due to the change in microstructure. The higher the value of η, the greater the energy used for dynamic recrystallization and the better workability can be obtained [39]. According to the extremum principles of irreversible thermodynamics, the instability map was established. The flow instability criterion is expressed as:

$$\xi(\dot{\varepsilon}) = \frac{\partial \ln\left(\frac{m}{m+1}\right)}{\partial \ln\dot{\varepsilon}} + m < 0 \tag{13}$$

The instability map was constituted by using variations of the instability parameter, temperature and the stain rate. The processing map is a superposition of the power dissipation map and instability map. The processing maps for the Cu-Mg-Fe-Ce and Cu-Mg-Fe alloys are presented in Fig. 8. The shaded domains represent the unstable region, which is at low temperature and high strain rate. The numbers on the contour lines represent the efficiency of power dissipation. As illustrated in Fig. 8(a) and (b), it is evident that the alloy with added rare earth element Ce has smaller instability region by comparing corresponding processing maps of the two alloys marked as C and C_1, respectively.

In addition, by observing the D, D_1 and D_2 three domains in Fig. 8, it

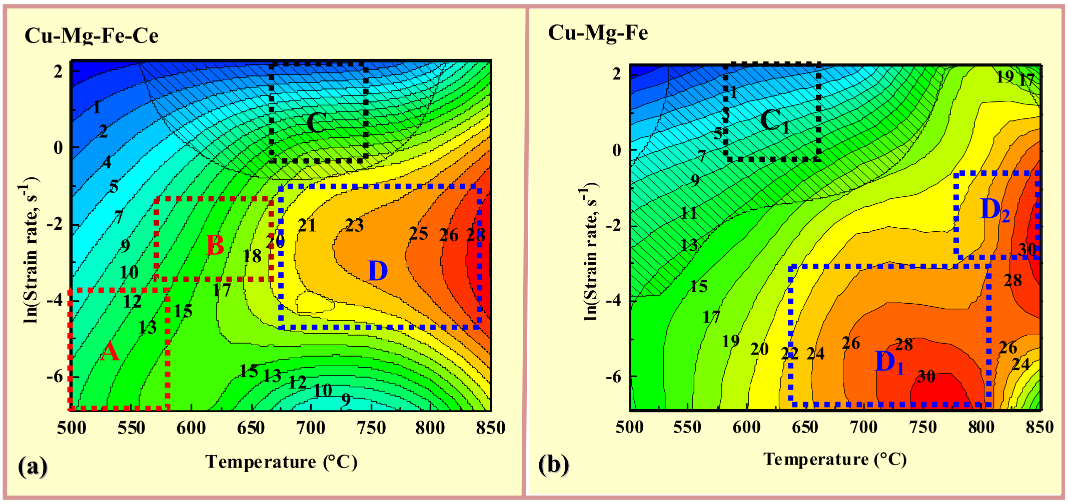

Fig. 8. Hot processing maps of: (a) Cu-Mg-Fe-Ce and (b) Cu-Mg-Fe alloys.

is easy to see that the regions with higher power dissipation value for the Cu-Mg-Fe-Ce alloy are mainly located at 675–850 °C with the strain rates ranging from 0.01 s^{-1} to 0.4 s^{-1}. There are two suitable areas for processing of the Cu-Mg-Fe alloy. One is 650–800 °C with the lower strain rates ranging from 0.001 s^{-1} to 0.01 s^{-1}, while the other is at 775–850 °C with the lower strain rates of 0.01–0.6 s^{-1}.

Fig. 9(a) represents the primary phase of hot deformation at 500 °C and 0.01 s^{-1} strain rate, which corresponds to the zone marked as A in Fig. 8(a). The grains are extensively elongated perpendicular to the compressed direction. Simultaneously, the shear bands originated at the grain boundaries. The appearance of shear bands often causes cracking of the workpieces, which should be avoided during real production. Meanwhile, the peak power dissipation value decreased by 3.3%, which indicates that the Cu-Mg-Fe-Ce alloy has less energy for dynamic recrystallization. Therefore, it can also explain that Ce delays dynamic recrystallization.

As shown in Fig. 9(b), the hot processing area is marked as B in Fig. 8(a). For instance, when Cu-Mg-Fe-Ce alloy deformed at 600 °C and 0.01 s^{-1}, crystal particles nucleate preferentially at grain boundaries and dynamic recrystallization grains extend gradually throughout the surrounding deformation matrix, which is a demonstration of the dynamic recrystallization, called the necklace tissue. This area should be avoided during hot working, because it is prone to crack initiation.

Furthermore, the shadow area is considered as the rheological instability region from 525 °C to 800 °C, marked as C in Fig. 8(a), with higher strain rates of 0.5–10 s^{-1}. Mixed crystal phenomenon is the remarkable feature of this stage, as illustrated in Fig. 9(c). This indicates that rheological instability is often accompanied by high strain rates [40,41]. The distribution of stress in the alloy is inhomogeneous and mainly concentrated at the interface, which will eventually lead to cracking. As for Fig. 9(d), the Cu-Mg-Fe-Ce alloy deformed at 850 °C with the strain rate of 0.1 s^{-1}, exhibits the growth of fine dynamic recrystallized grains, and equiaxed grains are observed. These results show that the microstructure of this stage is relatively stable with large power dissipation value. Microstructure of the Cu-Mg-Fe-Ce alloy deformed at 850 °C and 0.001 s^{-1} is shown in Fig. 9(e). Higher temperature and lower strain rate create an adequate phase transformation driving force and allow sufficient time for dynamic recrystallization, so the dynamic recrystallization grains grow completely.

Fig. 9(f) presents the microstructure of Cu-Mg-Fe alloy deformed at 850 °C with strain rate of 0.1 s^{-1}. It is seen that plenty of equiaxed grains disappeared. Nevertheless, some of the equiaxed grains have grown up in size and reached an average grain size of 16 μm. In Fig. 9(d) the average grain size of equiaxed grains of Cu-Mg-Fe-Ce alloy under the same condition is 10 μm. This implied that Ce contributes to the refinement of the recrystallized grains of the Cu-Mg-Fe alloy [8].

3.4. Deformation mechanism

Slip and twinning are the main mechanisms of metal plastic deformation. Metal with fcc structure has high symmetry accompanied by a large number of slip systems. Therefore, dislocation slip is the main mechanism. However, during hot deformation, twinning also occur under high temperature and low strain rate conditions. Wang et al. [42] found that the migration velocity of twinning mainly depends on the stacking fault energy. In addition, the appearance of twinning has an active effect on reducing stress concentration during tensile testing [43-45].

Crystal orientation will become favorable for slip, which is why plastic deformation occurs more easily. In addition, when the orientation of the crystal is unfavorable for dislocation sliding, twinning deformation will change the crystal orientation, so that slip can occur. Deformation subgrains with lower dislocation density are mainly continuously distributed in the dynamic recrystallization region. In the process of deformation, dislocations continue to proliferate, slip and distribute along the boundaries of subgrains or grains boundaries. Qin et al. [46] have confirmed that favorable nucleation sites for dynamic recrystallization are mainly provided by the large angle grain boundaries of 10–15°.

Fig. 10 shows TEM micrographs of the Cu-Mg-Fe and Cu-Mg-Fe-Ce alloys. As seen in Fig. 10(a) and (b), the difference between the Cu-Mg-Fe and Cu-Mg-Fe-Ce alloys deformed at 700 °C and 0.1 s^{-1} is the dislocation density. There are massive dislocations with higher density of the Cu-Mg-Fe-Ce alloy. By contrast, a large number of subgrains appear in the Cu-Mg-Fe alloy matrix instead. This also indicates that Ce delays the dynamic recrystallization. Fig. 10(c) describes the microstructure of the Cu-Mg-Fe-Ce alloy deformed at 850 °C and 0.1 s^{-1}. With the temperature increase, the dislocations further aggregated at grain boundaries or subgrain boundaries. The shadowed area in Fig. 10(c) marked as 1 shows dislocation nets. During this process, a large number of fine subgrains are grown in the grains, and the neighboring subgrains were continuously gathered, as shown in Fig. 10(c), marked as 1, 2 and 3. Thus the grains were refined. Meanwhile, the S type shear band is observed at the edge of the dislocation network, and the local strain also promotes the formation of subgrains. At this point, the dislocation density obviously decreases. A large number of precipitates can be seen from the TEM microstructure in Fig. 10(d) and (e). The precipitation aggregated at the grain boundary, which will nail the grain boundary.

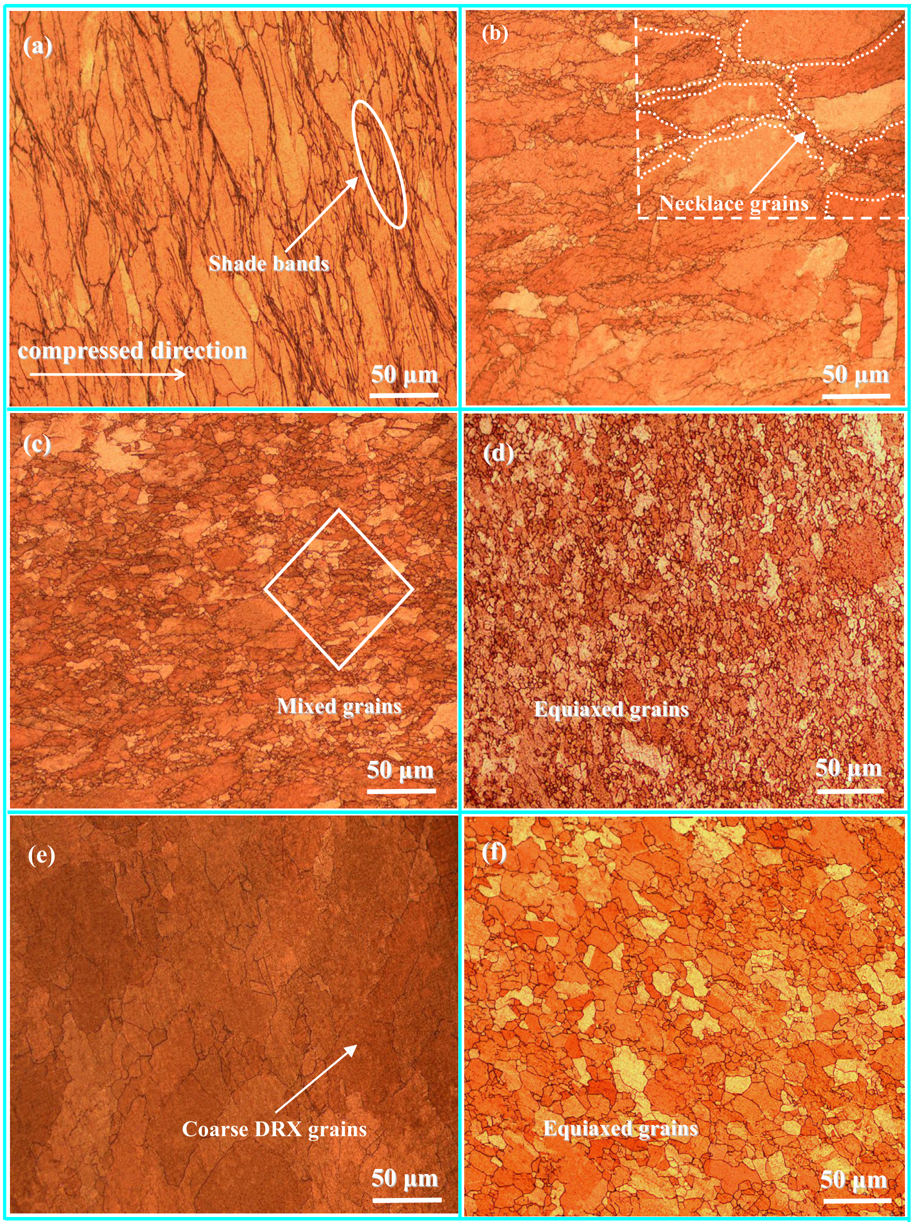

Fig. 9. Microstructure of the Cu-Mg-Fe-Ce alloy under different deformation conditions: (a) 500 °C, 0.01 s^{-1}; (b) 600 °C, 0.01 s^{-1}; (c) 700 °C, 1 s^{-1}; (d) 850 °C, 0.1 s^{-1}; (e) 850 °C, 0.001 s^{-1} and (f) Cu-Mg-Fe alloy deformed at 850 °C and 0.1 s^{-1}.

Movement of the grain boundary or subgrain boundary is blocked, thus impeding the deformation process. The diffraction spot is shown in Fig. 10(f). The precipitate was determined to be $CuMg_2$. When deformed at 850 °C and 0.01 s^{-1}, as illustrated in Fig. 10(d), many high-angle grains are observed, which indicates the completion of dynamic recrystallization. Meanwhile, twins are distributed uniformly at the edge of large angle grain boundaries. In Fig. 10(e) the number of twins obviously decreased, deformed at 850 °C and 0.001 s^{-1}. The main reason for this phenomenon may be when deformed at higher strain rate, there is less time for dislocations to move or the crystal orientation is unfavorable to start the dislocation source. Therefore, twinning dominates the deformation mechanism in the crystal. As mentioned above, the flow stress of the Cu-Mg-Fe-Ce alloy is prominently higher than the Cu-Mg-Fe alloy at the same conditions, partly due to the addition of Ce, another significant reason is the emergence of twins [47]. The twins structure reduces the dislocation slip of the average free path, thus effectively promoting hardening. Radetic [48] investigated the effects of deformation twining in the Cu-Ti alloy and confirmed that twins can produce aging hardening.

4. Conclusions

Hot deformation tests of the Cu-Mg-Fe and Cu-Mg-Fe-Ce alloys have been conducted in temperatures ranging from 500 °C to 850 °C and the 0.001–10 s^{-1} strain rate range. The following conclusions can be drawn from the experiments.

(1) The flow stress decreased with temperature and increased with the strain rate, mainly affected by the interaction of work hardening, dynamic softening and dynamic recrystallization.

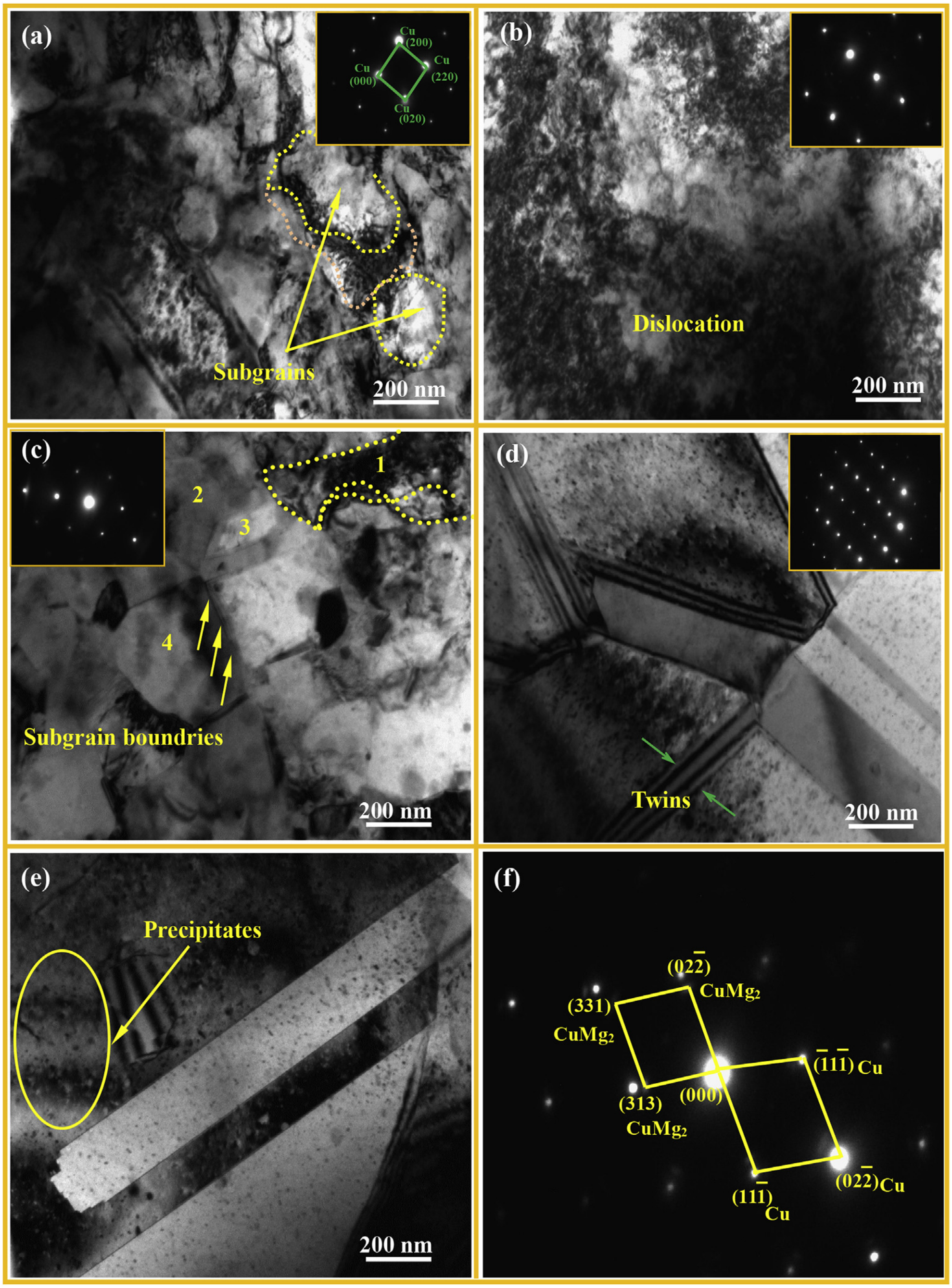

Fig. 10. TEM microstructure of: (a) Cu-Mg-Fe alloy and (b–e) Cu-Mg-Fe-Ce alloy deformed at different conditions: (a) 700 °C, 0.1 s^{-1}; (b) 700 °C, 0.1 s^{-1}; (c) 850 °C, 0.1 s^{-1}; (d) 850 °C, 0.01 s^{-1}; (e) 850 °C, 0.001 s^{-1}; (f) SAED pattern of Fig. 10(e).

(2) The addition of Ce effectively delayed dynamic recrystallization, refined the grains, increased the hardness of the Cu-Mg-Fe alloy by about 19%, and enhanced the peak stress of the Cu-Mg-Fe by about 7.3% deformed at 700 °C and 0.1 s^{-1} strain rate. Deformation activation energy of the Cu-Mg-Fe alloy was increased by about 25%. By multiple linear regressions, the constitutive equations of the Cu-Mg-Fe and Cu-Mg-Fe-Ce alloys were obtained as: $\dot{\varepsilon} = e^{25.612}[\sinh(0.013\sigma)]^{5.462}\exp\left(-\frac{255.3}{RT}\right)$ and $\dot{\varepsilon} = e^{34.591}[\sinh(0.010\sigma)]^{6.928}\exp\left(-\frac{323.7}{RT}\right)$, respectively.

(3) Based on the dynamic material model, processing maps were established for the Cu-Mg-Fe and Cu-Mg-Fe-Ce alloys. The optimal processing parameters for hot deformation of the Cu-Mg-Fe alloy are 650–800 °C with the lower strain rates 0.001–0.01 s^{-1} and 775–850 °C with the strain rates ranging from 0.01 s^{-1} to 0.6 s^{-1}, while for the Cu-Mg-Fe-Ce alloy the optimal processing parameters are 675–850 °C with the strain rates of 0.01–0.4 s^{-1}. Nevertheless, the rare earth element Ce narrowed the rheological instability region, which indicates that the addition of Ce promotes the thermal processing properties of the alloy, which can be more widely applied in production.

(4) Both slip and twinning occurred during hot deformation and were the main deformation mechanisms of DRX. Meanwhile, there was competition between them. Twinning controlled the DRX process at higher strain rate. Additionally, the precipitate observed in the Cu-Mg-Fe-Ce alloy deformed at 850 °C and 0.001 s^{-1} is determined to be $CuMg_2$.

Acknowledgements

This work was supported by the Henan University Scientific and Technological Innovation Talent Support Program (18HASTIT024), the National Natural Science Foundation of China (U1704143) and the National Science Foundation (IRES 1358088).

References

[1] Y. Zhang, B.H. Tian, A.A. Volinsky, X.H. Chen, H.L. Sun, Z. Chai, P. Liu, Y. Liu, Dynamic recrystallization model of the Cu-Cr-Zr-Ag alloy under hot deformation, J. Mater. Res. 31 (2016) 1275–1285.

[2] J.H. Su, Q.M. Dong, P. Liu, H.J. Li, B.X. Kang, Research on aging precipitation in a Cu-Cr-Zr-Mg alloy, Mater. Sci. Eng. 392 (2005) 422–426.

[3] L. Shen, Z. Li, Q. Dong, et al., Microstructure and texture evolution of novel Cu-10Ni-3Al-0.8Si alloy during hot deformation, J. Mater. Res. 31 (2016) 1113–1123.

[4] Y. Zhang, A.A. Volinsky, Hai T. Tran, Z. Chai, P. Liu, B.H. Tian, Effects of Ce addition on high temperature deformation behavior of Cu-Cr-Zr alloys, J. Mater. Eng. Perform. 24 (2015) 1–6.

[5] Y. Zhang, H.L. Sun, A.A. Volinsky, B.J. Wang, B.H. Tian, Y. Liu, K.X. Song, Constitutive model for hot deformation of the Cu-Zr-Ce alloy, J. Mater. Eng. Perform. 27 (2018) 728–738.

[6] J.Y. Dai, S.G. Mu, Y.R. Wang, X.P. Yang, J. Li, Influence of La and Ce on microstructure and properties of Cu-Cr-Zr Alloy, Adv. Mater. Res. 295–297 (2011) 1168–1174.

[7] X.B. Liu, P. Liu, S.G. Jia, B.H. Tian, Effects of trace Ce and Cr on properties of Cu-0.1Ag alloy, Heat Treat. Metals 30 (2005) 238–241.

[8] T. Du, Physical-chemical effect of rare earth elements on metallic materials, Acta Metall. Sin. 33 (1997) 69–77.

[9] M. Shaban, B. Eghbali, Determination of critical conditions for dynamic recrystallization of a microalloyed steel, Mater. Sci. Eng. 527 (2010) 4320–4325.

[10] Z.Y. Ding, S.G. Jia, P.F. Zhao, M. Deng, K.X. Song, Hot deformation behavior of Cu-0.6Cr-0.03Zr alloy during compression at elevated temperatures, Mater. Sci. Eng. 570 (2013) 87–91.

[11] K. Yu, W.X. Li, J. Zhao, Z.Q. Ma, R.C. Wang, Plastic deformation behaviors of a Mg-Ce-Zn-Zr alloy, Scripta Mater. 48 (2003) 1319–1323.

[12] C.M. Sellars, W.J. Mctegart, On the mechanism of hot deformation, Acta Metall. 14 (1966) 1136–1138.

[13] G.L. Ji, Q. Li, L. Li, A physical-based constitutive relation to predict flow stress for Cu-0.4Mg alloy during hot working, Mater. Sci. Eng. 615 (2014) 247–254.

[14] H. Mirzadeh, A. Najafizadeh, M. Moazeny, Flow curve analysis of 17-4 PH stainless steel under hot compression Test, Metall. Mater. Trans. 40 (2009) 2950–2958.

[15] H. Mirzadeh, A. Najafizadeh, Prediction of the critical conditions for initiation of dynamic recrystallization, Mater. Des. 31 (2010) 1174–1179.

[16] H. Mirzadeh, J.M. Cabrera, J.M. Prado, A. Najafizadehb, Hot deformation behavior of a medium carbon microalloyed steel, Mater. Sci. Eng. 528 (2011) 3876–3882.

[17] H. Mirzadeh, M.H. Parsa, Hot deformation and dynamic recrystallization of NiTi intermetallic compound, J. Alloy. Comp. 614 (2014) 56–59.

[18] S. Saadatkia, H. Mirzadeh, J.M. Cabrera, Hot deformation behavior, dynamic recrystallization, and physically-based constitutive modeling of plain carbon steels, Mater. Sci. Eng. 636 (2015) 196–202.

[19] T. Sakai, J.J. Jonas, Dynamic recrystallization: mechanical and microstructure considerations, Acta Metall. 32 (1984) 189–209.

[20] A. Rohatgi, K.S. Vecchio, G.T. Gray, The influence of stacking fault energy on the mechanical behavior of Cu and Cu-Al alloys: deformation twinning, work hardening, and dynamic recovery, Metall. Mater. Trans. 32 (2001) 135–145.

[21] Q. Lei, Z. Li, M.P. Wang, L. Zhang, S. Gong, Z. Xiao, Z.Y. Pan, Phase transformations behavior in a Cu-8.0Ni-1.8Si alloy, J. Alloy. Comp. 509 (2011) 3617–3622.

[22] Q. Li, Y.B. Xu, Z.H. Lai, L.T. Shen, Y.L. Bai, Dynamic recrystallization induced by plastic deformation at high strain rate in a monel alloy, Mater. Sci. Eng. 276 (2000) 250–256.

[23] T. Sakai, A. Belyakov, R. Kaibyshev, H. Miura, J.J. Jonas, Dynamic and post-dynamic recrystallization under hot, cold and severe plastic deformation conditions, Prog. Mater. Sci. 60 (2014) 130–207.

[24] H. Zhang, H.G. Zhang, L.X. Li, Hot deformation behavior of Cu-Fe-P alloys during compression at elevated temperatures, J. Mater. Eng. Perform. 209 (2009) 2892–2896.

[25] Y. Liu, Aging Precipitation Characteristics of high strength high electrical conductivity and trace alloyed Cu-Cr-Zr alloy contact wire, Doctoral Dissertations of Xi'an University of Technology, 2007.

[26] C. Bruni, A. Forcellese, F. Gabrielli, Hot workability and models for flow stress of NIMONIC 115Ni base super alloy, J. Mater. Process. Technol. 125 (2002) 242–244.

[27] C. Zener, J.H. Hollomon, Effect of strain-rate upon the plastic flow of steel, J. Appl. Phys. 15 (1994) 22–27.

[28] G.L. Ji, G. Yang, L. Li, Q. Li, Modeling constitutive relationship of Cu-0.4Mg alloy during hot deformation, J. Mater. Eng. Perform. 23 (2014) 1770–1779.

[29] H. Mirzadeh, M. Roostaei, M.H. Parsa, R. Mahmudi, Rate controlling mechanisms during hot deformation of Mg-3Gd-1Zn magnesium alloy: dislocation glide and climb, dynamic recrystallization, and mechanical twinning, Mater. Des. 68 (2015) 228–231.

[30] H. Mirzadeh, Constitutive description of 7075 aluminum alloy during hot deformation by apparent and physically-based approaches, J. Mater. Eng. Perform. 24 (2015) 1095–1099.

[31] H. Mirzadeh, Constitutive analysis of Mg-Al-Zn magnesium alloys during hot deformation, Mech. Mater. 77 (2014) 80–85.

[32] H. Mirzadeh, Simple physically-based constitutive equations for hot deformation of 2024 and 7075 aluminum alloys, Trans. Nonferrous Met. Soc. China 25 (2015) 1614–1618.

[33] H. Mirzadeh, Quantification of the strengthening effect of reinforcements during hot deformation of aluminum-based composites, Mater. Des. 65 (2015) 80–82.

[34] A. Shukla, N.M. Svs, S.C. Sharma, K. Mondal, Constitutive modeling of hot deformation behavior of vacuum hot pressed Cu-8Cr-4Nb alloy, Mater. Des. 75 (2015) 57–64.

[35] N. Liu, L. Zhou, G.Y. Xu, S.Q. Liang, Hot deformation behavior and cold workability of Cu-12Mn-13Zn-1Sn-1Al-0.1Si-0.1Ce alloy with white chromaticity, Mater. Sci. Eng. 553 (2012) 67–73.

[36] Y.T. Wu, Y.C. Liu, C. Li, X.C. Xia, Y. Huang, H.J. Li, Deformation behavior and processing maps of Ni_3Al-based superalloy during isothermal hot compression, J. Alloy. Comp. 712 (2017) 687–695.

[37] Y.V.R.K. Prasad, Author's reply: dynamic materials model: basis and principles, Metall. Mater. Trans. 27 (1996) 235–236.

[38] N. Srinivasan, Y.V.R.K. Prasad, P.R. Rao, Hot deformation behavior of Mg-3Al alloy-A study using processing map, Mater. Sci. Eng. 476 (2008) 146–156.

[39] Y. Zhang, A.A. Volinsky, Q.Q. Xu, C. Zhe, B.H. Tian, P. Liu, H.T. Tran, Deformation behavior and microstructure evolution of the Cu-2Ni-0.5Si-0.15Ag alloy during hot compression, Metall. Mater. Trans. 46 (2015) 5871–5876.

[40] L. Xu, L. Chen, G.J. Chen, M.Q. Wang, Hot deformation behavior and microstructure analysis of 25Cr3Mo3NiNb steel during hot compression tests, Vacuum 147 (2018) 8–17.

[41] D.X. Wen, Y.C. Lin, Y. Zhou, A new dynamic recrystallization kinetics model for a Nb containing Ni-Fe-Cr-base superalloy considering influences of initial δ phase, Vacuum 141 (2017) 316–327.

[42] J. Wang, N. Li, O. Anderoglu, X. Zhang, A. Misra, J.Y. Huang, J.P. Hurth, Detwinning mechanisms for growth twins in face-centered cubic metals, Acta Mater. 58 (2010) 2262–2270.

[43] Y. Chino, K. Kimura, M. Mabuchi, Twinning behavior and deformation mechanisms of extruded AZ31 Mg alloy, Mater. Sci. Eng. 486 (2008) 481–488.

[44] Y.N. Wang, J. Huang, The role of twinning and untwinning in yielding behavior in hot-extruded Mg-Al-Zn alloy, Acta Mater. 55 (2007) 897–905.

[45] D. Brown, S.R. Agnew, M. Bourke, C.N. Tomé, Internal strain and texture evolution during deformation twinning in magnesium, Mater. Sci. Eng. 399 (2005) 1–12.

[46] F.M. Qin, H. Zhu, Z.X. Wang, X.D. Zhao, W.W. He, H.Q. Chen, Dislocation and twinning mechanisms for dynamic recrystallization of as-cast Mn18Cr18N steel, Mater. Sci. Eng. 684 (2017) 634–644.

[47] S.J. Mu, F. Tang, G. Gottstein, A cluster-type grain interaction deformation texture model accounting for twin-induced texture and strain-hardening evolution: application to magnesium alloys, Acta Mater. 68 (2014) 310–324.

[48] T. Radetic, V. Radmilovic, W.A. Soffa, Electron microscopy observations of deformation twinning in a precipitation hardened copper-titanium alloy, Scripta Mater. 35 (1996) 1403–1409.